Springer

Available online at https://link.springer.com/journal/42241
http://www.jhydrodynamics.com
Journal of Hydrodynamics, 2022, 34(5): 806-825
https://doi.org/10.1007/s42241-022-0068-6

Studying turbulence structure near the wall in hydrodynamic flows: An approach based on the Schur decomposition of the velocity gradient tensor

Christopher J. Keylock*
School of Architecture, Building and Civil Engineering, Loughborough University, Leicestershire, UK

(Received August 23, 2022, Revised August 31, 2022, Accepted September 12, 2022, Published online November 3, 2022)

Abstract: The Schur decomposition of the velocity gradient tensor (VGT) is an alternative to the classical Cauchy-Stokes decomposition into rotation rate and strain rate components. Recently, there have been several strands of work that have employed this decomposition to examine the physics of turbulence dynamics, including approaches that combine the Schur and Cauchy-Stokes formalisms. These are briefly reviewed before the latter approach is set out. This partitions the rotation rate and strain rate tensors into normal/local and non-normal/non-local contributions. We then study the relation between the VGT dynamics and ejection-sweep events in a channel flow boundary-layer. We show that the sweeps in particular exhibit novel behaviour compared with either the other quadrants, or the flow in general, with a much-reduced contribution to the dynamics from the non-normal terms above the viscous sub-layer. In particular, the reduction in the production term that is the interaction between the non-normality and the normal straining reduces in the log-layer as a consequence of an absence of alignment between the non-normal vorticity and the strain rate eigenvectors. There have been early forays into using the Schur transform approach for subgrid-scale modelling in large-eddy simulation (LES) and this would appear to be an exciting way forward.

Key words: Turbulence, channel flow, velocity gradient tensor, Schur decomposition

Introduction

While we may not always engage explicitly with turbulence processes in hydrodynamics, for any Newtonian flow with a significant amount of inertia we need at the very least to make a conscious decision to ignore such phenomena. Arguably, this is precisely the approach of traditional hydraulic engineering–to derive the momentum and continuity equations assuming an inviscid behaviour and to then add in a friction coefficient to deal with energy and momentum losses due to processes that include turbulence dissipation.

However, reach-scale studies concerning civil engineering design (e.g., scour around bridge piers), sediment transport or channel ecology are increasingly using computational fluid dynamics (CFD) methods[1]. Either these require a closure model for the fluctuating velocities or at least their covariance, as arises in Reynolds-Averaged Navier Stokes (RANS) methods, or the larger scales are fully resolved in time and it is the smaller scales that require modelling, as arises in large-eddy simulation (LES). (See various review papers on the application of LES to hydrodynamics and related fields[2-5]).

In the classical closure model employed in LES[6], an expression is written for a sub-filter scale viscosity with a length scale related to the geometric mean of the filter size, $l_f = (l_x l_y l_z)^{1/3}$, and a time scale linked to the resolved rate of strain tensor

$$\nu_f = (C_S l_f)^2 \left\| \tilde{S} \right\| \tag{1}$$

where C_S is the Smagorinsky coefficient, the tilde indicates the LES filtering operation, $\| \ \|$ is the Frobenius norm, i.e.

$$\left\| \tilde{S} \right\| = \sqrt{2 \tilde{S}_{ij} \tilde{S}_{ij}} \tag{2}$$

and

$$\tilde{S}_{ij} = \frac{1}{2} \left(\frac{\partial \tilde{u}_i}{\partial x_j} + \frac{\partial \tilde{u}_j}{\partial x_i} \right) \tag{3}$$

This demonstrates the direct relevance of the gradients

Biography: Christopher J. Keylock, Male, Ph. D., Professor
Corresponding author: Christopher J. Keylock,
E-mail: c.j.keylock@lboro.ac.uk

in the flow to modelling in hydrodynamics. Thus, while the velocities are generally associated to large-scale behaviour and the velocity gradients with the small scales, understanding the small scales has a direct impact on our formulation of hydrodynamics at a variety of scales.

The aim of this article is to review some recent work in fluid mechanics in this area and discuss its potential for enhancing our understanding of hydrodynamical flows before presenting some new results on the boundary-layer structure of a channel flow. In 2005, Iehisa Mezu outlined what he felt should be the focus for the research direction in the 21st century in hydraulic engineering and he highlighted the significance of turbulence representation, primarily from the perspective of Reynolds-averaged dynamics (the focus of his experimental work for several decades)[7]. A decade ago, Adrian and Marusic suggested instead that the focus instead should be on the transient flow field and the associated coherent flow structures that are responsible for a significant proportion of the turbulent stresses in many hydrodynamic flows[8]. Associated more with this latter perspective, as part of the 50th anniversary special issue of Water Resources Research we argued that the hydrodynamics' disciplines should take a more active role in shaping their own "fluvial fluid mechanics"[9] rather than drawing upon developments in turbulence theory made in other subject areas.

The current article proposes a research direction to underpin this idea. In particular, of the work developing our understanding of velocity gradients since a major review article on this topic[10], a strand of particular interest has emerged based on the Schur decomposition of the velocity gradient tensor. It would appear that the first publication in this area, although it did not refer to the Schur transform explicitly, was published in Chinese by Li et al. in 2014[11]. Four years later, studies emerged at a very similar time from Liu's group in Arlington, Texas in the USA, in China, and also in the UK[12-15]. Despite the same underpinning linear algebra, the various studies are rather distinct, with emphasis on flow structure identification in the work of Liu et al., the physics of actual flows in Keylock's work, and underpinning physical principles in the work of Zhu. In this article, we consider all three strands of work, but focus on our own contribution as we believe the flow physics highlighted are potentially of greatest interest to the hydrodynamics' community and are of utility to the development of practical modelling closures of use in hydrodynamics.

In the next section we review some of the classic approaches to analysing the velocity gradient tensor and how the mathematics of the decomposition may be interpreted in terms of flow physics. In section 2 we look at the Schur decomposition and briefly describe some of the results so far using this approach. In section 3 we provide some new results on the near-wall dynamics of channel flow in the logarithmic, and transitional regions of the boundary-layer using this approach to demonstrate its utility. The final section looks at how these ideas may be developed to both enhance our understanding of flow dynamics and improve our ability to model hydrodynamical flows in the future.

1. Classic concepts in velocity gradient dynamics

1.1 *The velocity gradient tensor and its invariants*

The natural way to think about these velocity gradients is in terms of the velocity gradient tensor (VGT)

$$A_{ij} = \frac{\partial u_i}{\partial x_j} \tag{4}$$

which is classically decomposed in fluid mechanics into two tensors, the rotation rate and strain tensors (i.e., from a mathematical perspective, a decomposition into Hermitian, skew-Hermitian elements):

$$\Omega_{ij} = \frac{1}{2}\left(\frac{\partial u_i}{\partial x_j} - \frac{\partial u_j}{\partial x_i}\right), \quad S_{ij} = \frac{1}{2}\left(\frac{\partial u_i}{\partial x_j} + \frac{\partial u_j}{\partial x_i}\right) \tag{5}$$

For compactness, it is often convenient to re-express Eq. (5) using matrix/tensor notation as

$$\boldsymbol{\Omega}_A = \frac{1}{2}(\boldsymbol{A} - \boldsymbol{A}^*), \quad \boldsymbol{S}_A = \frac{1}{2}(\boldsymbol{A} + \boldsymbol{A}^*) \tag{6}$$

where the asterisk is the transpose operation.

Considering the tensor from the perspective of linear algebra opens up some alternative ways of representing the flow in contrast to the strain and rotation approach. Perhaps the first thing one can do is to write down the characteristic equation for the VGT

$$\lambda_i^3 + P\lambda_i^2 + Q\lambda_i + R = 0 \tag{7}$$

where λ_i are the eigenvalues of $\boldsymbol{A}$. This equation simplifies for incompressible flow because $P = -\sum \lambda_i = 0$. While analysis of the compressible VGT is important in a number of domains of fluid mechanics and, consequently, has been the focus of some study[16-17], in this article we assume that for hydrodynamics the overwhelming concern is with incompressible dynamics.

The second and third invariants may be written as

$$Q = -\frac{1}{2}\mathrm{tr}(\boldsymbol{A}^2) \equiv (1-\delta_{ij})\sum \lambda_i \lambda_j \tag{8}$$

$$R = -\det(\boldsymbol{A}) \equiv \Pi \lambda_i \tag{9}$$

where $\mathrm{tr}(\cdots)$ is the trace, δ_{ij} is the Kronecker delta and $\det(\cdots)$ is the determinant. Of these pair of terms, the one most familiar to hydrodynamicists will be Q as it is the term employed in the Q-criterion approach to flow structure identification[18], which has been widely used in hydrodynamics[19-21]. However, it is useful to treat them as a pair because, in combination they define the discriminant function, Δ, that establishes if the eigenvalues of the VGT are all real $(\Delta \le 0)$ or consist of a real value and a conjugate pair $(\Delta > 0)$

$$\Delta = Q^3 + \frac{27}{4}R^2 \tag{10}$$

In the latter case, the streamlines in a Lagrangian frame form a closed streamline, explaining why Δ is sometimes also used as a means to detect coherent structures[22]. A more physically intuitive interpretation of the second and third invariants is obtained by rewriting Eqs. (8), (9) as:

$$Q = \frac{1}{2}(\|\boldsymbol{\Omega}_A\|^2 - \|\boldsymbol{S}_A\|^2) \tag{11}$$

$$R = -\det(\boldsymbol{S}_A) - \mathrm{tr}(\boldsymbol{\Omega}_A^2 \boldsymbol{S}_A) \tag{12}$$

where the first and second terms on the right-hand side of Eq. (11) are commonly referred to as the enstrophy and total strain, respectively, while the first and second terms on the right-hand side of Eq. (12) are the strain production and enstrophy production, respectively.

While both the constituents of Q in Eq. (11) are non-negative, this is not the case for R, although observations in a variety of flows indicate that this is the most common situation. In fact, the relative balance of the signs of the terms on the right-hand side of Eq. (12) is very dependent upon the region of the joint probability distribution function (PDF) for Q and R that the VGT is located in (see Fig. 1). For example, for homogeneous, isotropic turbulence at a Taylor Reynolds number of 430, Keylock[12] found that 63.4% of all VGTs had values for both of the production terms that were positive, but that this was most common in both absolute and relative terms for region 6 ($Q<0$, $\Delta<0$ and $R>0$), (30.2% of all tensors were in region 6, 87% of these had both production terms positive). In contrast, 11.1% of tensors arose in region 1 ($Q>0$ and $R>0$) and only 16% of the tensors had both production terms positive. A physical consequence of the general positivity of the strain production is that the eigenvalues for the strain rate tensor, e_i, are preferentially two positive and one negative value rather than vice versa. In other words, they yield disc-shaped straining structures in the flow, rather than tube-shaped[23-24]. The implication of this is that the mechanics of turbulent dissipation are associated with the compression of disc-shaped elements, rather than the stretching of tube-shaped structures[25].

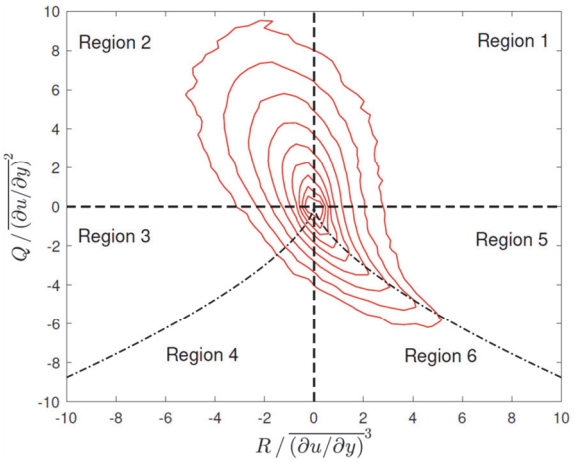

Fig. 1 (Color online) The Q-R diagram, i.e., the joint distribution function for Q and R obtained for a turbulent channel flow at a distance from the wall of $20 \le y^+ \le 30$. The six regions of this diagram are identified based on the signs of Q, R (dashed lines) and the discriminant function, Δ (dot-dashed lines). Contours show the base 10 logarithm of the probabilities with contours ranging from –4.5 to 0.5 in intervals of 0.5

1.2 *The Q-R diagram and turbulence structure*

Going into greater detail into aspects of the Q-R diagram, the example in Fig. 1 is from the simulation used later in this study and is taken from the top of the transitional region into the bottom of the logarithmic layer in a turbulent channel flow $(20 \le y^+ \le 30)$, where the plus superscript indicates the use of wall units (non-dimensionalisation of distance by kinematic viscosity and shear velocity). It is clear that even this close to the wall and below a height where the flow can be considered to be fully established, the Q-R diagram already exhibits classical features

such as the extended Vieillefosse tail[26] along $\Delta = 0$ for positive R, i.e., spanning regions 5, 6. This teardrop shape is so well-known for fully developed flow that it has been argued that its occurrence can be used as a verification test for turbulence resolving numerical simulations[27].

Exactly how the shape of the diagram changes with the imposition of coherent flow structures and as a function of the manner in which turbulence develops is very much an area for active research. For example, it was shown that both round and fractal jet flows attained the teardrop shape at a distance of approximately $x/D_e = 25$ from the nozzle, where D_e is the equivalent jet diameter, while for the case of a spatially evolving mixing layer, the equivalent distance was $x/D_{sp} = 225$, where D_{sp} is the splitter plate thickness[28].

An example of direct relevance to the understanding of channel flows in hydrodynamics is a classic study of how the boundary-layer ejection-sweep structure related to the regions of the Q-R diagram in a low Reynolds number boundary-layer[29]. These authors found that ejections ($u' < 0$, $v' > 0$) arose preferentially in region 5, and sweeps ($u' > 0$, $v' < 0$) in region 6, where u and v are the longitudinal and vertical velocity components and the prime indicates the fluctuating (mean-subtracted) part. In other words, these coherent motions in the turbulent boundary-layer are not related directly to the regions where enstrophy exceeds total strain (regions 1 and 2), and thus, the coherent flow structures themselves if one uses the definition $Q > 0$ [18]. Chacin and Cantwell also showed that dissipation events in the viscous sublayer ($y^+ < 5$) were preferentially in regions 3, 4 and 6, with a shift to dominance by region 6 in the transitional and logarithmic regions. It is this examination of the relation between the flow quadrants (ejections, sweeps, outward and inward interactions) and the velocity gradient tensor that we investigate below from the perspective of the Schur transformed flow field.

1.3 *Modelling the velocity gradient tensor*

Taking the first derivative of the Navier-Stokes momentum equation yields an evolution equation for the VGT

$$\frac{\partial}{\partial t}(A_{ij}) + u_k \frac{\partial}{\partial x_k}(A_{ij}) + A_{ik}A_{kj} = -\frac{1}{\rho}\frac{\partial^2 p}{\partial x_i \partial x_j} + \nu \frac{\partial^2 A_{ij}}{\partial x_k \partial x_k} \tag{13}$$

It is then useful to subtract the isotropic part of the pressure Hessian from the full form. We can do this by using incompressibility (i.e., $A_{ii} = 0$) to state that $A_{ik}A_{ki} = -(\rho^{-1})\partial^2 p / \partial x_i \partial x_i$ and to then subtract this from Eq. (13) to obtain

$$\frac{\partial}{\partial t}(A_{ij}) + u_k \frac{\partial}{\partial x_k}(A_{ij}) + A_{ik}A_{kj} - \frac{\delta_{ij}}{3}(A_{km}A_{mk}) = -\frac{1}{\rho}\left[\frac{\partial^2 p}{\partial x_i \partial x_j} - \frac{\delta_{ij}}{3}\frac{\partial^2 p}{\partial x_k \partial x_k}\right] + \nu \frac{\partial^2 A_{ij}}{\partial x_k \partial x_k} \tag{14}$$

The primary reason to write the equation this way follows from the work of Cantwell[30] who showed that by neglecting the terms on the right-hand side of Eq. (14) one may obtain a simple model for the evolution of the second and third invariants:

$$\frac{\mathrm{d}Q}{\mathrm{d}t} = -3R, \quad \frac{\mathrm{d}R}{\mathrm{d}t} = \frac{2}{3}Q^2 \tag{15}$$

The solutions to this model are either that the VGT remains at the origin, or that it follows lines of constant Δ to $Q = -\infty$, $R = \infty$. Thus, one would anticipate that the Q-R diagram has a mode at the origin and would be asymmetric, with an extended tail in the bottom-right corner. This is precisely what is observed in Fig. 1.

It is clear that Eq. (15) only requires knowledge of the second and third invariants and, thus, from Eqs. (8), (9), the eigenvalues. Given that the full dynamics are more complex that this model, the implication is that evidence for effects related to the deviatoric pressure Hessian, the term in the square brackets in (14), must reside in the eigenvectors. It is this observation that motivated the application of the Schur decomposition to the VGT by Keylock[12] because, as shown in the next section, the Schur decomposition makes these terms physically explicit.

2. The Schur decomposition of the VGT

An ideal matrix decomposition should be unitary, diagonalisable and orthogonal. There is a trade-off in trying to accomplish all three and while the Schur and eigen decompositions are both orthogonal (and are identical for symmetric tensors), the eigen decomposition is always diagonalisable while the Schur decomposition is always unitary. In effect, this means that there is a simpler structure to the rotation matrices for the Schur decomposition. The eigen decomposition of $\boldsymbol{A}$ is

$$\boldsymbol{V}\boldsymbol{\lambda}\boldsymbol{V}^{-1} = \boldsymbol{A} \tag{16}$$

where the columns of $\boldsymbol{V}$ are the eigenvectors and $\boldsymbol{\lambda}$

is a diagonal matrix of eigenvalues, λ_i. In contrast, the Schur decomposition is

$$\boldsymbol{UTU}^{*}=\boldsymbol{A} \tag{17}$$

where $\boldsymbol{T}$ is no longer typically diagonal but is block upper triangular in the real form and upper triangular in the complex form. In the special case where $\boldsymbol{A}$ is symmetric, there is no non-normality, $\boldsymbol{T}$ is diagonal and equivalent to $\boldsymbol{\lambda}$ and the Schur rotation matrix, $\boldsymbol{U}$, is equivalent to the eigenvector matrix, $\boldsymbol{V}$. While other authors have adopted the real form of the Schur transform because of its ease of physical interpretation[13, 31], here we adopt the complex variant because of the ease of separation of the normal (the eigenvalues on the diagonal) and non-normal (the upper triangular part) components[12], which is at the heart of this paper. It should be noted that when $\Delta<0$ there is no imaginary part to the complex Schur decomposition and the real and complex forms are identical. Assuming that the Jordan block for the real form is in the top-left corner, the complex form and real forms for the Schur decomposition may be written, respectively, as:

$$\boldsymbol{T}=\begin{bmatrix}\lambda_c & \gamma_c & \beta_c\\ 0 & \lambda_c & \alpha_c\\ 0 & 0 & \lambda_r\end{bmatrix} \tag{18}$$

and

$$\boldsymbol{T}_R=\begin{bmatrix}\lambda_{cr} & \psi+\gamma & \beta\\ -\psi & \lambda_{cr} & \alpha\\ 0 & 0 & \lambda_r\end{bmatrix} \tag{19}$$

For an incompressible flow, $\lambda_r=-2\lambda_{cr}$, where the "cr" subscript indicates the real part of the complex eigenvalue of the VGT, λ_c, while λ_r is the real eigenvalue. We recover the imaginary part of the complex eigenvalues, λ_{ci} from Eq. (19) by noting that $2\lambda_{ci}^2+\gamma_{cr}^2+\gamma_{ci}^2=2\psi^2+2\psi\gamma+\gamma^2$ and $\gamma_{cr}^2+\gamma_{ci}^2=\gamma^2$. That the imaginary part of the eigenvalues resides off the diagonal in the real form and is mixed with γ is why we have used the complex form as it permits the simple separation

$$\boldsymbol{T}=\boldsymbol{\lambda}+\boldsymbol{N} \tag{20}$$

The derived dynamical terms (which involve taking the trace and determinant) are all real-valued as shown below. The equivalence between the eigen- and Schur decompositions for symmetric tensors demonstrates that when the tensors are non-symmetric, information that is "hidden" in the eigenvectors with the eigen decomposition is made physically explicit in $\boldsymbol{N}$. The simplicity of the separation in Eq. (20) permits us to write[12]:

$$\boldsymbol{A}=\boldsymbol{B}+\boldsymbol{C},\quad \boldsymbol{B}=\boldsymbol{U\lambda U}^{*},\quad \boldsymbol{C}=\boldsymbol{UNU}^{*} \tag{21}$$

Hence, $\boldsymbol{B}$ captures the normal terms associated with the eigenvalues, $\boldsymbol{C}$ the non-normal terms in $\boldsymbol{N}$ associated with the dynamic effects of the deviatoric part of the pressure Hessian. Hence, in relation to the discussion in the concluding paragraph of the previous section, the effects missing from the restricted Euler formalism Eq. (15) that are not due to viscous effects may be found in $\boldsymbol{C}$. Using an analysis of the pressure terms in the VGT[32] it can then be shown that the non-normal part of the tensor represents the non-local actions of the surrounding flow field on the local VGT.

2.1 *Subgrid-scale modelling based on the Schur decomposition*

Using the Schur transform to make explicit the contributions to equations Eqs. (1)-(3) from local and non-local terms is clearly of significant potential utility in hydrodynamics given the need to model small scales based on large-scale information. In fact, an early attempt has emerged from China that attempts to do this for compressible boundary-layers[33]. These authors adopted the index κ_{BC} [12]

$$\kappa_{BC}=\frac{\|\boldsymbol{B}\|-\|\boldsymbol{C}\|}{\|\boldsymbol{B}\|+\|\boldsymbol{C}\|} \tag{22}$$

as a means to determine the relative contributions of the normal and non-normal terms with distance from a solid boundary. They showed significant differences in the vertical profiles of the second and third invariants when conditioned on the sign of κ_{BC}. For example, Q was weakly positive on average for $\kappa_{BC}<0$ with a maximum at $y^{+}\sim 150$, while Q was strongly negative for $\kappa_{BC}>0$, with a minimum at $y^{+}=10$ and then a recovery towards zero at higher y^{+}. Conversely, R was weakly negative for $\kappa_{BC}>0$ (minimum at $y^{+}=100$) and strongly positive for $\kappa_{BC}<0$, with a maximum at $y^{+}=30$. This led to the observation that near the wall ($y^{+}=24$) subgrid-scale energy dissipation was a strong function of κ_{BC}, with the dissipation for

$\kappa_{BC} = -0.3$ approximately three times greater than for $\kappa_{BC} = 0.3$. As a consequence, the authors were able to propose a new subgrid-scale model with a separation of the straining into its $\boldsymbol{B}$ and $\boldsymbol{C}$ components. This was able to replicate the direct numerical simulation more appropriately than the classic Smagorinsky closure, while also respecting the test filtering concept that permits the subgrid-scale model coefficients to vary spatially and temporally[34].

2.2 *Physics elucidated using the Schur decomposition of the VGT*

Given the decomposition in Eq. (21) it is then, of course possible to rewrite (11)-(14) in terms of $\boldsymbol{B}$, $\boldsymbol{C}$ and study the dynamics associated with the new terms that result[12]. If this is done then Q and R may be written in terms of $\boldsymbol{B}$, as follows from their definition in terms of the eigenvalues as seen in Eqs. (8), (9). In other words, $\boldsymbol{B}$ contains the rotational and straining dynamics associated with the eigenvalues. In the special case of a symmetric VGT, all the dynamics are strain rates associated with the eigenvalues, i.e., $\boldsymbol{A} = \boldsymbol{S}_B$. However, more generally, and particularly in the boundary-layers studied in this paper, the VGT can be strongly asymmetric as a consequence of shearing in the flow inducing torques on a fluid element. Such motions are not captured by the eigenvalues but are found in the non-normal tensor, $\boldsymbol{C}$. These may then in turn be decomposed into symmetric straining and rotational components. The constituents of Q and R that appear in Eqs. (11), (12) cannot be expressed solely in terms of the eigenvalues. Hence, we write the enstrophy and the total strain as:

$$\|\boldsymbol{\Omega}_A\|^2 = \|\boldsymbol{\Omega}_B\|^2 + \|\boldsymbol{\Omega}_C\|^2, \quad \|\boldsymbol{S}_A\|^2 = \|\boldsymbol{S}_B\|^2 + \|\boldsymbol{\Omega}_C\|^2 \tag{23}$$

With regards to the constituents of R, we have that

$$-\det(\boldsymbol{S}_A) = -\det(\mathbf{S}_B) + \mathrm{tr}(\boldsymbol{\Omega}_C^2\boldsymbol{S}_B) - \det(\boldsymbol{S}_C),$$

$$\mathrm{tr}(\boldsymbol{\Omega}_A^2\boldsymbol{S}_A) = \mathrm{tr}(\boldsymbol{\Omega}_B^2\boldsymbol{S}_B) + \mathrm{tr}(\boldsymbol{\Omega}_C^2\boldsymbol{S}_B) - \det(\boldsymbol{S}_C) \tag{24}$$

where we have used $\|\boldsymbol{\Omega}_C\|^2 = \|\boldsymbol{S}_C\|^2$ to simplify the number of terms. Thus, four of the terms in these two equations are the direct, normal analogues of the traditional terms. The three new terms are the non-normality, $\|\boldsymbol{\Omega}_C\|^2$, the interaction production, $\mathrm{tr}(\boldsymbol{\Omega}_C^2\boldsymbol{S}_B)$, i.e., production of non-normality by action of the normal straining, and the non-normal production, $-\det(\boldsymbol{S}_C)$.

The non-normality, $\|\boldsymbol{\Omega}_C\|^2$, is typically at least as large as the normal total strain or normal enstrophy. For example, it has been shown for homogeneous, isotropic turbulence (HIT) that the only region of the Q-R diagram where the mode for κ_{BC} is positive is region 6[12]. The mode is close to zero in region 1 and negative in the other regions. Non-normality is most dominant in region 3. In other words, traditional analyses in terms of the eigenvalues of $\boldsymbol{A}$ miss out more than half of the relevant dynamical effects. A mathematical consequence of the decomposition is that the normal enstrophy, $\|\boldsymbol{\Omega}_B\|^2$, is necessarily zero in regions 4, 6 of the Q-R diagram (where $\Delta < 0$). In other words, any non-zero values for $\|\boldsymbol{\Omega}_A\|^2$ in these regions arise solely because of the non-normality. Furthermore, while both $-\det(\boldsymbol{S}_A)$, $\mathrm{tr}(\boldsymbol{\Omega}_A^2\boldsymbol{S}_A)$ are typically positive in well-developed flows, the signs of their normal variants are dictated by the sign of R. Thus, in regions 1, 5 and 6 where $R > 0$, we have that $-\det(\boldsymbol{S}_B) > 0$ and $\mathrm{tr}(\boldsymbol{\Omega}_B^2\boldsymbol{S}_B) < 0$, with the opposite true where $R < 0$. Of course, in regions 4 and 6, because of the absence of the normal enstrophy, the exact value for R follows directly from the simplification, $R = -\det(\boldsymbol{S}_B)$.

In terms of the statistical distribution functions for the two new production terms, it was shown that the marginal distribution for $-\det(\boldsymbol{S}_C)$ is symmetric about a mean of zero and this is also true for the conditional distributions of this term as a function of $\mathrm{tr}(\boldsymbol{\Omega}_C^2\boldsymbol{S}_B)$. In contrast, the marginal distribution for $\mathrm{tr}(\boldsymbol{\Omega}_C^2\boldsymbol{S}_B)$ was shown to be clearly positive in the mean. Given the imbalance between positive and negative values for R is relatively small, it therefore follows that the positivity of $\mathrm{tr}(\boldsymbol{\Omega}_C^2\boldsymbol{S}_B)$ is what drives the positive values for the strain production and enstrophy production.

An important discovery about the small-scale dynamics of turbulence was that the vorticity vector aligned with the eigenvector corresponding to the intermediate eigenvalue of the strain rate tensor, $\boldsymbol{S}_A$ [35-36]. This was not expected as one might anticipate that it would align with either the extensive or the compressive direction, given the topological explanations for turbulence dissipation[37-38]. The reason for this discrepancy is because of the way the argument prioritises the normal terms. In fact, in regions 1 and 2 where normal enstrophy is large, one does find a strong alignment between the normal vorticity vector and either the most extensive (region 2) or most compressive (region 1) normal strain eigenvector. However, the strongest alignment in the other regions concern the non-normal terms, and here, this is always

between $\boldsymbol{\omega}_C$ and the intermediate eigenvector for $\boldsymbol{S}_C$ [12]. With $\|\boldsymbol{\Omega}_C\|^2 > \|\boldsymbol{\Omega}_B\|^2$ in regions 3-6 and because the intermediate strain eigenvectors for both $\boldsymbol{S}_B$ and $\boldsymbol{S}_C$ are strongly aligned, the net effect is the intermediate alignment between $\boldsymbol{\omega}_A$ and $\boldsymbol{S}_A$.

In regions 1, 2, while $\boldsymbol{\omega}_A$ aligns with either the first or third eigenvector for the normal strain rate, this term is typically small from the definition of Q. In fact, in regions 1, 2, these two eigenvectors were themselves strongly aligned to the intermediate eigenvector for the non-normal straining, leading to the intermediate alignment between $\boldsymbol{\omega}_A$ and $\boldsymbol{S}_A$ via a different mechanism[12].

While the results described above were for HIT there have been subsequent studies highlighting the importance of the non-normal terms, particularly as turbulence is developing or evolving. In addition to work on compressible boundary-layers[33], Beaumard and co-workers looked at how κ_{BC} evolved from strongly negative to more positive values in spatially developing flows[28], while a more recent study of multiphase flows found that κ_{BC} was more strongly negative close to the interface between the fluid species[39]. In a hydrodynamics context, this implies that, for example, in locations of high Froude number, where air entrainment is commonplace, closure models that operationalise equations for the local and non-local straining separately, in the spirit of the work by Yu et al.[33] will be advantageous.

Once one makes use of $\boldsymbol{N}$ in an analysis of fluid mechanical systems, one can begin to study the manner in which this term is bounded based on knowledge of other aspects of the flow. Employing the Lee bound[40], which is tight for incompressible flow, one can isolate the tensors that lie close to this bound[41] (the practical definition used in that work was within 0.01% of the Lee bound). It is not of interest to study this bound in regions 4, 6 of the Q-R diagram (where $\Delta < 0$) because it is attained trivially. However, where the eigenvalues are complex this is not the case and it was discovered that the probability of attaining the Lee bound was much greatest in region 1 as a consequence of the typical values for the interaction production and non-normal production terms and the vorticity-strain eigenvector alignments being much more similar in this region to the values for when the bound was attained than in regions 2, 3 and 5. Lagrangian tracking showed that the bound was obtained as the tensors transitioned from region 2 into region 1, i.e., where the normal enstrophy production and strain production values are small. A topological investigation showed these regions to be typically rod-like in shape, with an average spacing of about 0.7 Taylor length scales, and a typical intermediate axis length of 0.25 Taylor scales.

In contrast to the work described above, an alternative avenue has been to take a more mathematical approach and formulate a real Schur form for the dynamics that is equivalent to a two component, two-dimensional flow coupled to a one component, three-dimensional flow[15] when the Jordan block is in the top-left corner. This type of fluid dynamics is seen most clearly at the Taylor-Proudman limit for rotating, compressible flows, when the flow forms columnar structures[42-43]. This was exploited to argue for a mechanism of "turbulence compressibility reduction" based on the approach to an incompressible state for the two-dimensional, two component part of the flow in the limit of fast rotation[43]. There is a richer class of behaviours in the compressible case due to the thermodynamic, barotropic and non-barotropic structure. There is some fascinating mathematical physics in this work, although in order for any insights from these cases to be of direct relevance to conventional hydrodynamics rather than, for example, geophysical fluid dynamics and the analysis of Bose-Einstein condensates some thought needs to be given to the way in which the rotation tensor is integrated into the flow reconstruction. In our approach[12, 28], the observed $\boldsymbol{U}$ is used directly. It would be interesting to explore the manner in which a real Schur flow changes in nature as one moves from a universal, constant, $\boldsymbol{U}$ towards one that is unique to every point in time and space by introducing some periodic variation in $\boldsymbol{U}$ as a function of position and scale. This is very much an unexplored area at present.

2.3 *Coherent flow structure identification using the Schur decomposition*

In a series of papers, Liu, Gao and co-workers have developed an approach to coherent flow structure identification using the Schur transform[13-14, 44] that incorporates an idea also seen in Li et al.'s work[11] regarding the decomposition of the VGT. We first present this work using the notation of Liu et al., before relating it back to the Schur transform approach adopted by Li et al. At the heart of the formulation by Liu and co-workers is an initial rotation from the x, u system in Eq. (13) to one in X, U such that rotation is only around the Z axis, i.e., the new VGT is

$$\boldsymbol{A} = \begin{bmatrix} \dfrac{\partial U}{\partial X} & \dfrac{\partial U}{\partial Y} & 0 \\ \dfrac{\partial V}{\partial X} & \dfrac{\partial V}{\partial Y} & 0 \\ \dfrac{\partial W}{\partial X} & \dfrac{\partial W}{\partial Y} & \dfrac{\partial W}{\partial Z} \end{bmatrix} \tag{25}$$

A second re-orientation is then undertaken to find the local rotation strength, i.e., with θ the angle applied, then the rotation matrix is

$$\boldsymbol{\Theta}=\begin{bmatrix} \cos\theta & \sin\theta & 0 \\ -\sin\theta & \cos\theta & 0 \\ 0 & 0 & 1 \end{bmatrix} \tag{26}$$

leading to the new tensor $\boldsymbol{A}_\theta = \boldsymbol{\Theta}\boldsymbol{A}\boldsymbol{\Theta}^*$. The two relevant terms in $\boldsymbol{A}_\theta$ for describing the rotation strength are then

$$\left.\frac{\partial V}{\partial X}\right|\theta = n_1\sin(2\theta+\varphi)+n_2\,,\quad \left.\frac{\partial U}{\partial y}\right|\theta = n_1\sin(2\theta+\varphi)-n_2 \tag{27}$$

where

$$n_1 = \frac{1}{2}\sqrt{\varepsilon_1^2+\varepsilon_2^2}\,,\quad n_2 = \frac{1}{2}\varepsilon_3 \tag{28}$$

with

$$\varepsilon_1 = \frac{\partial V}{\partial Y}-\frac{\partial U}{\partial X}\,,\quad \varepsilon_2 = \frac{\partial V}{\partial X}+\frac{\partial U}{\partial Y}\,,\quad \varepsilon_3 = \frac{\partial V}{\partial X}-\frac{\partial U}{\partial Y} \tag{29}$$

and the phase adjustment, φ, depends on the sign of the ε terms:

$$\varphi = \tan^{-1}\left(\frac{\varepsilon_2}{\varepsilon_1}\right) \text{ if } \varepsilon_1 \neq 0 \tag{30a}$$

$$\varphi = \frac{\pi}{2} \text{ if } \varepsilon_1 = 1\,,\ \varepsilon_2 > 0 \tag{30b}$$

$$\varphi = -\frac{\pi}{2} \text{ if } \varepsilon_1 = 1\,,\ \varepsilon_2 < 0 \tag{30c}$$

It is then possible to define the rotation strength, R_L, as

$$R_L = 2(n_2-n_1) \text{ if } n_1^2-n_2^2<0\,,\ n_2>0 \tag{31a}$$

$$R_L = 2(n_2+n_1) \text{ if } n_1^2-n_2^2<0\,,\ n_2<0 \tag{31b}$$

$$R_L = 0 \text{ if } n_1^2-n_2^2\geq 0 \tag{31c}$$

Thus, a coherent structure is a connected region where $R_L>0$ and it is possible to define an accompanying vector field (initially termed the Rortex[14] and, subsequently referred to as the Liutex[45]) according to $\boldsymbol{L} = R_L\boldsymbol{r}$, where

$$\boldsymbol{r} = \boldsymbol{U}^*\begin{bmatrix} 0 \\ 0 \\ 1 \end{bmatrix} \tag{32}$$

The above mathematics simplifies greatly if we use the Schur form[11]. Noting that Eq. (25) is the transpose of the real Schur form in Eq. (19), we adopt Eq. (19) in place of Eq. (25), which forces $\varepsilon_1 = 0$, $\varphi = \pm\pi/2$ depending on the sign of γ (because $\varepsilon_2 \equiv \gamma$). With $\varepsilon_2 = 2\varphi+\gamma$, we may rewrite n_1, n_2 as

$$n_1 = \frac{1}{2}\gamma\,,\quad n_2 = \varphi+\frac{1}{2}\gamma \tag{33}$$

and the three cases in Eq. (31) correspond to ψ, $\psi+\gamma$ and 0, respectively. However, the second of these is inadmissible as it requires $n_2<0$ and there are two possibilities when using the Schur form: The eigenvalues are real and $\psi = 0$, meaning that although $n_2<0$ is possible, $n_1^2 = n_2^2$, and therefore, $R_L = 0$; or, $-\psi$ and $\psi+\gamma$ in Eq. (19) are opposite in sign (reflecting the signs of the imaginary parts of the conjugate pair eigenvalues) then with $\psi>0$ by definition and $\psi+\gamma>0$, n_2 must also be positive.

A particular advantage of this approach to coherent flow structure identification compared to other techniques is that in addition to the scalar R_L, one has access to an accompanying vector field, $\boldsymbol{r}$, which is different to other metrics such as Q or λ_{ci}. In addition, this vector field has been found to respect the orientation of the coherent flow structures in contrast to, for example, the vorticity. This is demonstrated very effectively in Fig. 4 of the study by Gao and Liu[14].

While Liu and co-workers were initially more concerned with using this decomposition to enhance the identification of coherent flow structures, more recently their work has taken a direction towards the flow kinematics of the VGT. Their approach has been to focus on tensor decomposition[11] rather than the separation and reconstruction approach we formulated. The elements of the decomposition are the Liutex tensor, a shearing tensor, and a stretching/compression tensor. Each of these has its own principal coordinate system, although recent progress to towards deriving this decomposition within the original coordinate system[46] aligns this more closely with our work. Hence, it will be interesting to explore the relative

merits and demerits of these two formulations in future research.

3. Analysis of near-wall flow in a channel flow boundary-layer

The aim of this section is to examine the quadrant events in the boundary-layer of a turbulent channel flow and the manner in which they couple to the VGT dynamics, including the invariants and regions of the Q-R diagram, as originally studied by Chacin and Cantwell[29], and the new terms in Eqs. (23), (24). Quadrants have been used for many years for analysing boundary-layer structure[47-48] and are formed from the longitudinal, u and vertical, v, velocity components because, in a fully developed boundary layer, fluctuations in the transverse plane are only weakly correlated to the other directions. However, of course, with the complex boundaries found in natural channels, this assumption may break down and tracking the sequence of the resulting flow "octants" that include the transverse component has been shown to be useful for studying near-wall flow structure and its relation to sediment entrainment[49].

The additional advantage of quadrants is they may be related directly to the Reynolds decomposition of the flow field and, thus, the representation of turbulence in RANS models. With the mean velocity at a point denoted by an overbar, the Reynolds decomposition states that the instantaneous velocity, u is the sum of the mean and a fluctuating component denoted by a prime, e.g.

$$u = \overline{u} + u' \tag{34}$$

Based on the sign of u' and v' we then have the nomenclature for quadrants given in Table 1. In this study we normalise the results by the product of the standard deviations of the velocity components at a given y^+. Hence, one may compare the magnitude of the velocity covariance to the product of the standard deviations, with significant flow events, being those that exceed a threshold hole size, H_T [48], i.e., $|u'v'| > H_T \sigma_u \sigma_v$ for an event to occur. We choose H_T empirically below before relating these quadrants to the structure of the VGT.

Table 1 Definitions of the quadrant events used to characterise boundary-layer flow structure

Designation	Name	u'	v'
q1	Outward interactions	+	+
q2	Ejections	–	+
q3	Inward interactions	–	–
q4	Sweeps	+	–

3.1 *The simulation employed*

In this study we make use of the Johns Hopkins Turbulence database channel flow simulation[50-51]. This is a direct numerical simulation of a wall-bounded flow with periodic boundary conditions in the longitudinal and transverse directions[52]. No slip conditions are imposed at the top and bottom walls and the flow was initially driven to maintain a bulk velocity of $U = 1$ until stationarity was achieved. A mean pressure gradient giving the same shear stress as the previous step was then imposed, with the equations solved using the PoongBack code[53]. Data were stored at 2 048×512×1 536 spatial positions for a domain size of $8\pi h \times 2h \times 3\pi h$, with h the channel half height. Thus, the computational cells had a spacing of $x^+ = 12.26$ and $z^+ = 6.13$ wall units in the longitudinal and transverse directions, respectively. The wall-normal spacing varied from $y^+ = 0.02$ for the first node from the wall to $y^+ = 6.16$ for the nodes at the centre-line. The shear velocity Reynolds number was $Re_\tau = u_\tau h / \nu = 1\,000$, with a bulk velocity Reynolds number of $Re = Uh / \nu = 20\,000$ and a kinematic viscosity of $\nu = 5 \times 10^{-5}$ (dimensionless). The best-fit mean velocity profile attained the law-of-the-wall for $30 \le y^+ \le 250$ [50]. Given the observation that the differences between the local and non-local dynamics are more pronounced for $y^+ < 100$ [33], coupled to the fact that it is this region where the subgrid-scale model typically has to represent a significant proportion of the dynamics in hydrodynamics' LES unless one is using an exhorbitant amount of computer power, in this study we focus on the lower part of the logarithmic region and below.

3.2 *A suitable hole size for ejection-sweep events*

In order to couple the quadrant motions in the boundary-layer to the behaviour of the VGT, one first needs to empirically define the threshold "hole size", H_T, for quadrant identification. Figure 2 indicates the proportion of events that arise as a function of H_T at four different heights: Just above the viscous sub-layer $(y^+ = 10)$, in the middle of the transitional region $(y^+ = 20)$, at the bottom of the log-layer $(y^+ = 30)$ and higher into the logarithmic region $(y^+ = 65)$. Based on these results it is suggested that $H_T = 1$ is a suitable threshold as the general tendencies in the data are established by this point in all panels, and this is also compatible with the choice in other studies[54-55]. In addition, a higher threshold would result in fewer events to analyse, particularly the inward interactions and outward interactions.

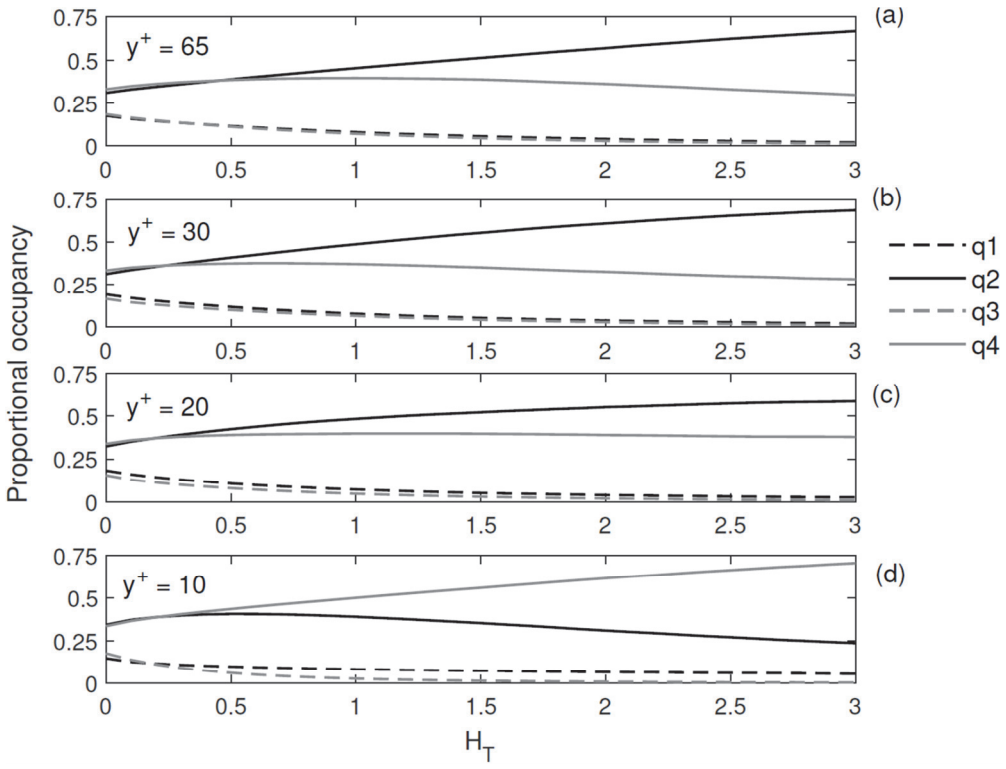

Fig. 2 The proportion of the data occupied in each quadrant as a function of the hole size, H_T for four choices of y^+

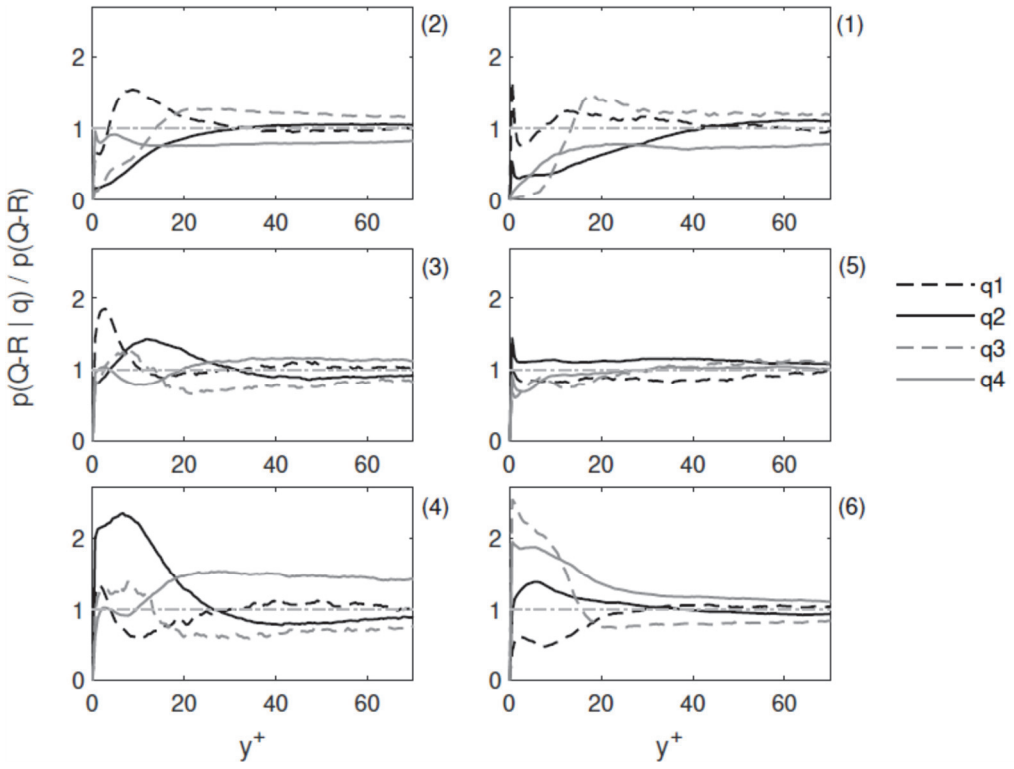

Fig. 3 The frequency of each region (panels) of the Q-R diagram conditioned on a given quadrant occurrence relative to the frequency of occurrence for each region, as a function of y^+. The horizontal, grey, dash-dotted line indicates the average state, $p(Q\text{-}R|q)\,/\,p(Q\text{-}R)=1$

3.3 *The relation between quadrants and the Q-R diagram*

Figure 3 shows the relative frequency of each region of the Q-R diagram conditioned on each quadrant occurrence. The sweeps (q4) occur more frequently than the flow in general in regions 4, 6 and in the former this is particularly the case for $y^+ > 20$, as the logarithmic region becomes established. Ejections (q2) are more frequent than the flow in general throughout the near-wall region in region 5 consistent with previous work[29] However, there is also a clear vertical structure to the behaviour of the ejections, with a peak in regions 6, 4 for $y^+ < 10$, a maximum at $5 < y^+ < 20$ in region 3, values exceeding unity in regions 1, 2 once $y^+ > 30$ and then the general preferential occurrence in region 5. In other words, within the viscous sub-layer ejections originate with minimal local vorticity, gain some initial local vorticity in the transitional region $5 < y^+ < 20$ where local enstrophy production is positive and then in regions 1, 2, where enstrophy exceeds total strain, ejections arise preferentially in the log-layer. Thus, in addition to the well-known result that sweeps occur preferentially in region 6 and ejections in region 5[29], our results show that in the log-layer we have strain-dominated sweeps in region 4 and enstrophy-dominated ejections in regions 1 and 2, with also a contribution from inward interactions (q3) in regions 1 and 2.

Overall, the highest relative frequencies of all are associated with inward interactions in region 6 for $y^+ < 10$, while these q3 events also have a relative frequency greater than 1 in the log-layer for regions 1 and 2. The implication of this is that the inward interactions are more closely related to the sweeps near the wall and the ejections in the logarithmic region. The outward interactions (q1) are important in regions 2 and 3 where there is some local enstrophy and where local enstrophy production is positive. They occur underneath the ejections in these regions such that the outward interactions peak in the viscous sub-layer in region 3 and at $y^+ \sim 10$ in region 2.

3.4 *The relative importance of the normal and non-normal contributions near the wall*

Median values for κ_{BC} as a function of distance from the wall are given in Fig. 4. Each panel gives the results for a different region of the Q-R diagram and it is very clear that in all panels κ_{BC} values are strongly negative and increase with y^+ (i.e., the normal contributions from $\boldsymbol{B}$ increase in importance with distance from the wall). Nearly all the median values for each quadrant and each region lie close to, but just below zero by the time one is well into the log-layer at $y^+ = 70$. Beyond this height, the results do not exhibit much variation and are not shown. The sweeps (grey lines) deviate from the general pattern for the quadrants, with values close to zero regions 4 and 6 where sweeps are of particular importance to the dynamics. In other words, in a channel flow, non-normal effects near the wall are dominant with the exception of the sweeps in the high strain rate, low enstrophy regions for $y^+ > 30$.

Looking at results for the sweeps in more detail, for regions 3-6 it is clear that for $y^+ \leq 5$ the κ_{BC} values for the sweeps are very close to -1 but at $y^+ \sim 10$ there is a sudden transition such that, by $y^+ = 20$, the κ_{BC} values for the sweeps are much greater than for the other quadrants. In the enstrophy dominated regions 1 and 2 where sweeps are rare, this tendency is much weaker and the sweeps are similar to the outward and inward interactions. This behaviour may be contrasted with the ejections that exhibit the least non-normality on average for $y^+ < 10$ for most regions, but once into the log-layer at $y^+ > 30$ exhibit the greatest non-normality. This is consistent with the classic model of the ejections being generated locally in the viscous sub-layer and then reflecting the characteristics of the surrounding flow as they are transported away from the wall. In contrast, sweeps originate away from the wall and therefore are dominated by non-local dynamics for $y^+ < 10$.

Moving away from an index of non-normality to a physical quantity, we define Φ as the extent to which the normal second order terms dominate the dynamics

$$\Phi = \frac{1}{2}(\|\boldsymbol{\Omega}_B\|^2 + \|\boldsymbol{S}_B\|^2) - \|\boldsymbol{\Omega}_C\|^2 \tag{35}$$

We can then non-dimensionalise Φ and Q by the square of the mean shear rate, $(\overline{\partial u/\partial y})^2$. Figure 5 shows the joint distribution function for Q and Φ for $60 < y^+ < 70$ for each quadrant (black lines in each panel) as well as the dataset as a whole (dashed, grey lines that are consistent between panels). As with the traditional Q-R diagram, these results highlight the non-Gaussian nature of the joint PDF, but here the source is different: rather than being a consequence of the Vieillefosse tail, it is driven by the suppression of normality close to $Q = 0$. This manifests itself as a re-entrant angle for the joint PDF on the positive Φ side and enhanced probabilities for $-\Phi$ values at

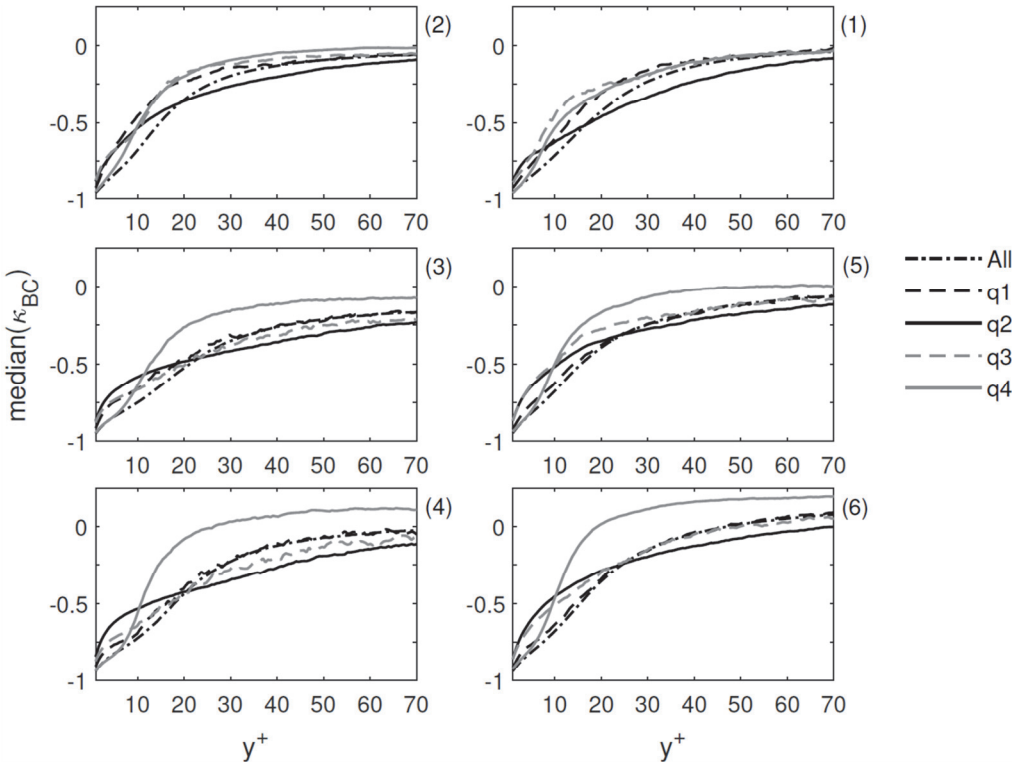

Fig. 4 The median values for κ_{BC} as a function of y^+ and each region (panels) of the Q - R diagram. In each panel, results are shown for all data (dot-dashed line) as well as the four quadrants in the ejection-sweep cycle

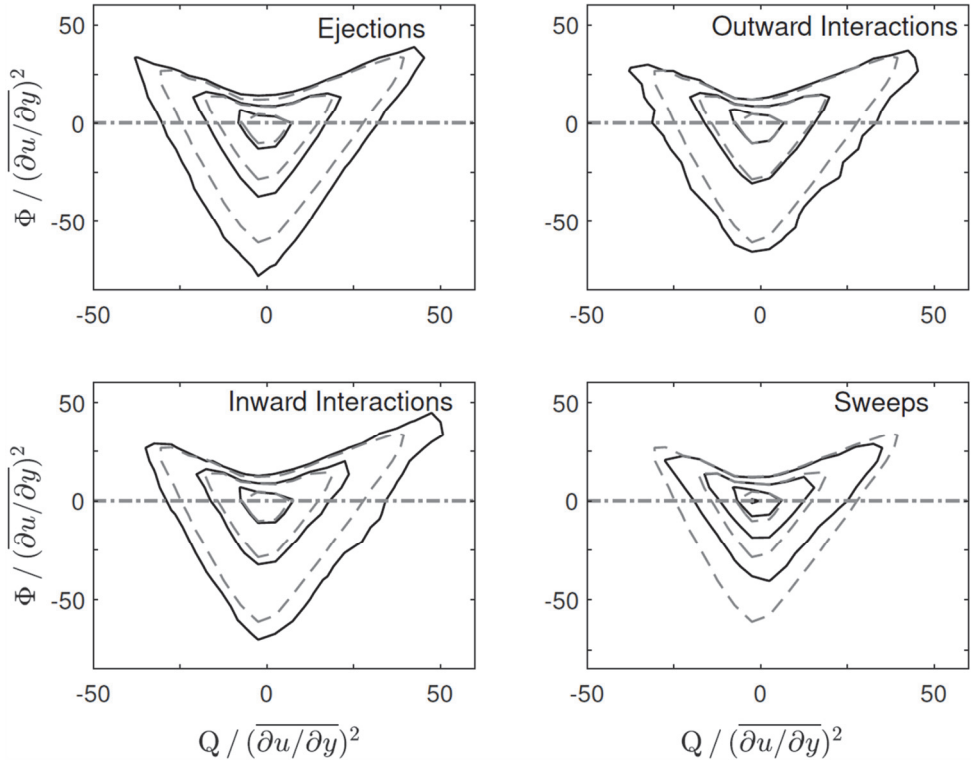

Fig. 5 The joint PDFs for Q and Φ for the four quadrants (black lines) for $60 \leq y^+ \leq 70$. Results are shown for the base 10 logarithms of the probabilities with contours from −5 to −3 in unit increments. The results shown by a grey dashed line in each panel are the results for the full dataset over this range of distances from the wall. The $\Phi = 0$ state is highlighted by the dot-dashed line

$Q \sim 0$. This is true to some extent in all cases, but the exceptional quadrant, as also seen in Fig. 4, is the sweeps. These exhibit a similar probability structure close to $Q = 0$ for all data on the positive Φ side but have a much reduced likelihood of negative Φ values. In addition on the negative Q side there is also a contraction to the contours that weakens as Φ increases. In other words, sweeps are more common in negative Q regions and exhibit less non-normality than the flow in general, consistent with Fig. 4. Given the result that dissipation is most likely in region 6 where sweeps are common[29], and given the low magnitude for the velocity gradients for the sweeps as seen in Fig. 5, the clear implication is that the sweeps themselves are not contributing directly to the dissipation for $60 < y^+ < 70$. The other three quadrants are much more similar in their behaviour in Fig. 5, which is also in agreement with Fig. 4. The asymmetry in these diagrams is associated with a tail to the distribution at $Q > 0$, $\Phi > 0$, i.e., normal dynamics are more likely to be coupled to regions 1 and 2 than the other regions of the Q-R diagram.

How the structure for Q-Φ emerges in the transitional region can be seen in Fig. 6, where it is very clear that for the data as a whole there is a very strong concentration of values for $-\Phi$ and $Q \sim 0$ in the transitional region at $20 < y^+ < 30$. This is respected for the quadrants in general, but certainly not for the sweeps, where the distribution is truncated in this part of the diagram to a greater relative extent than seen higher into the flow. Thus, the major change in the logarithmic region compared to the transitional region is the reduction in this association between non- normality and Q values close to zero. In the positive Φ half of the diagram we see in Fig. 6 that the outward interactions have an excess probability for $Q > 0$, while for the ejections and sweeps this occurs for $Q < 0$, and for the inward interactions appears to be the case for any of the strong magnitude Q events irrespective of sign.

3.5 *Third order terms and the ejection-sweep cycle*

Figure 7 shows the joint PDF for the sum of the two normal production terms (y-axis) and the non-normal and interaction production terms (x-axis) at $60 < y^+ < 70$. Again, the most notable feature is the behaviour of the sweeps, in particular, the contraction in the probabilities for values close to zero on the axis involving the normal terms (the y-axis). Furthermore, it is then also the case that the outward interactions and inward interactions exhibit characteristics more similar to the ejections, particularly with an enhanced probability in the top-right region-large values for normal production are associated with enhanced interaction and non-normal production. The key difference between the ejections and the other quadrants is that production is greater for ejections than the flow in general. The exception is when the sum of the normal production terms (y-axis) is negative, whereupon the sum of interaction production and non-normal production (x-axis) is not really any greater than the flow in general. When the two normal terms are approximately equal (i.e., $R \sim 0$) is where the combined interaction and non-normal production terms exhibit the greatest magnitude of excess compared to the flow in general.

In order to understand the processes arising on the x-axis of Fig. 7 in greater detail, Fig. 8 shows the joint PDF for the interaction production and non-normal production as a function of the different quadrants. In agreement with previous work[12] we see that the distribution for $-\det(\boldsymbol{S}_C)$ is more symmetrical than that for the interaction production, meaning it is the latter that drives the positive skew for the x-axis seen in Fig. 7. The contraction of the joint PDF for the sweeps observed in the previous figures is also seen here, particularly for positive interaction production. This implies that either (1) the normal straining or (2) the non-normality are reduced in magnitude for the sweeps, or (3) there is a reduction in the strength of the alignment between the non-normal vorticity vector and the normal straining eigenvectors. That (1) is correct is improbable given that sweeps arise preferentially in regions 4 and 6 (Fig. 3) where normal straining dominates normal enstrophy. We have seen in Fig. 5 that the non-normality is certainly reduced in magnitude for the sweeps, meaning that (2) must be part of the explanation. However, if this was the sole reason then one would anticipate the reduction in $-\det(\boldsymbol{S}_C)$ at $\mathrm{tr}(\boldsymbol{\Omega}_C^2\boldsymbol{S}_B) = 0$ to be at least as great as the reduction in $\mathrm{tr}(\boldsymbol{\Omega}_C^2\boldsymbol{S}_B)$ where $-\det(\boldsymbol{S}_C) = 0$ in Fig. 8 given that $-\det(\boldsymbol{S}_C)$ involves the non-normality to the third order and the interaction production to the second order.

With the eigenvalues for the normal strain rate tensor given by e_i, ordered from most positive to most negative, and with $\boldsymbol{e}_i$ the corresponding eigenvectors, then θ_i^{CB} is the angle between the non-normal vorticity vector, $\boldsymbol{\omega}_C$, the ith eigenvector of $\boldsymbol{S}_B$, Fig. 9 shows values for $\cos(\theta_i^{CB})$ for $60 < y^+ < 70$ as a function of the region of the Q-R diagram for all the data, as well as for the ejections and sweeps. As previously discussed for incompressible flow, in regions 1, 2, 3 and 5 where the

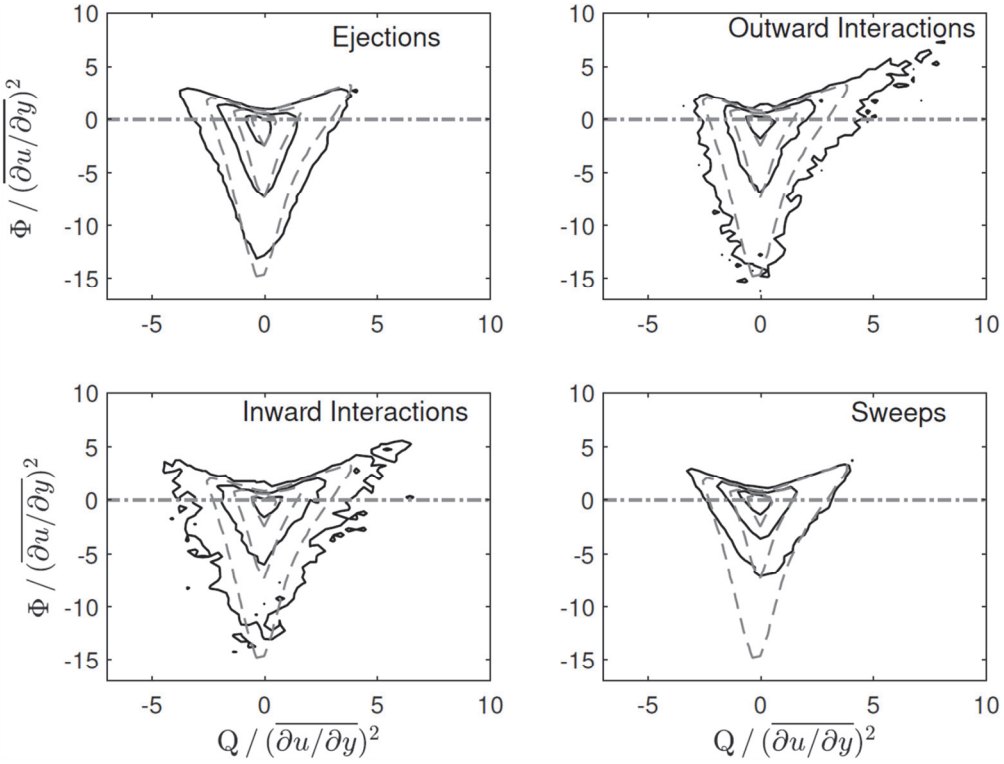

Fig. 6 The joint PDFs for Q and Φ for the four quadrants (black lines) for $20 \leq y^+ \leq 30$. Results are shown for the base 10 logarithms of the probabilities with contours from −3 to −1 in unit increments. The results shown by a grey dashed line in each panel are the results for the full dataset over this range of distances from the wall. The $\Phi = 0$ state is highlighted by the dot-dashed line

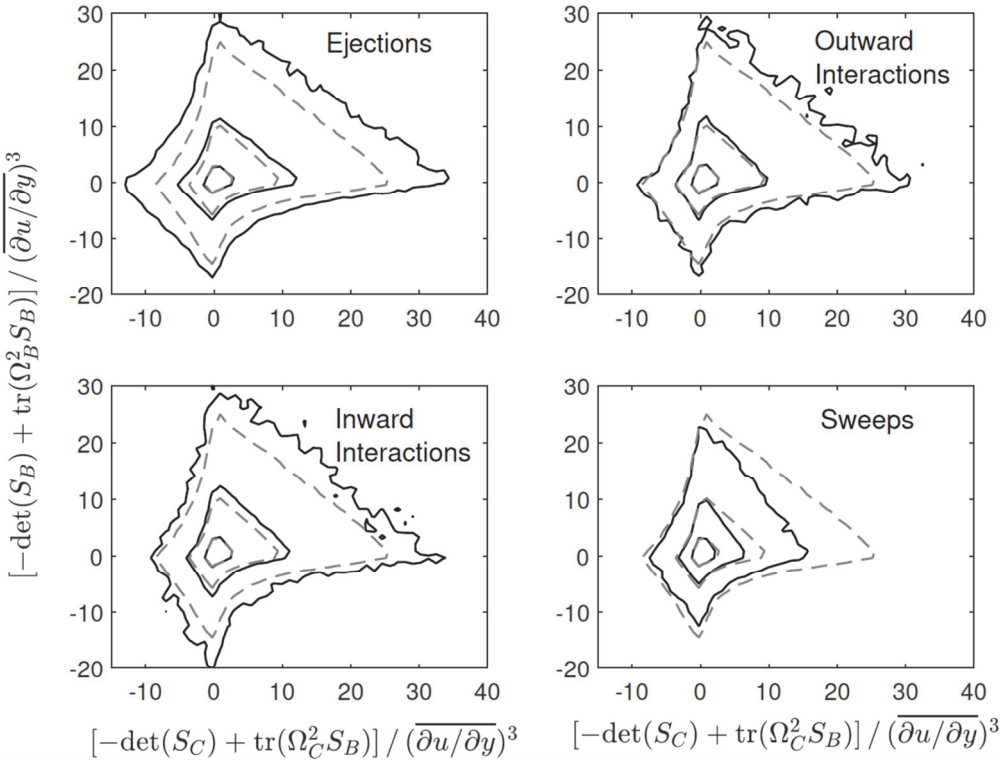

Fig. 7 The joint PDFs for sum of the normal and non-normal production terms for $60 \leq y^+ \leq 70$. Results are shown for the base 10 logarithms of the probabilities with contours from −4 to −2 in unit increments and each panel shows the results for the quadrants (solid, black lines) as well as all the data (grey, dashed lines)

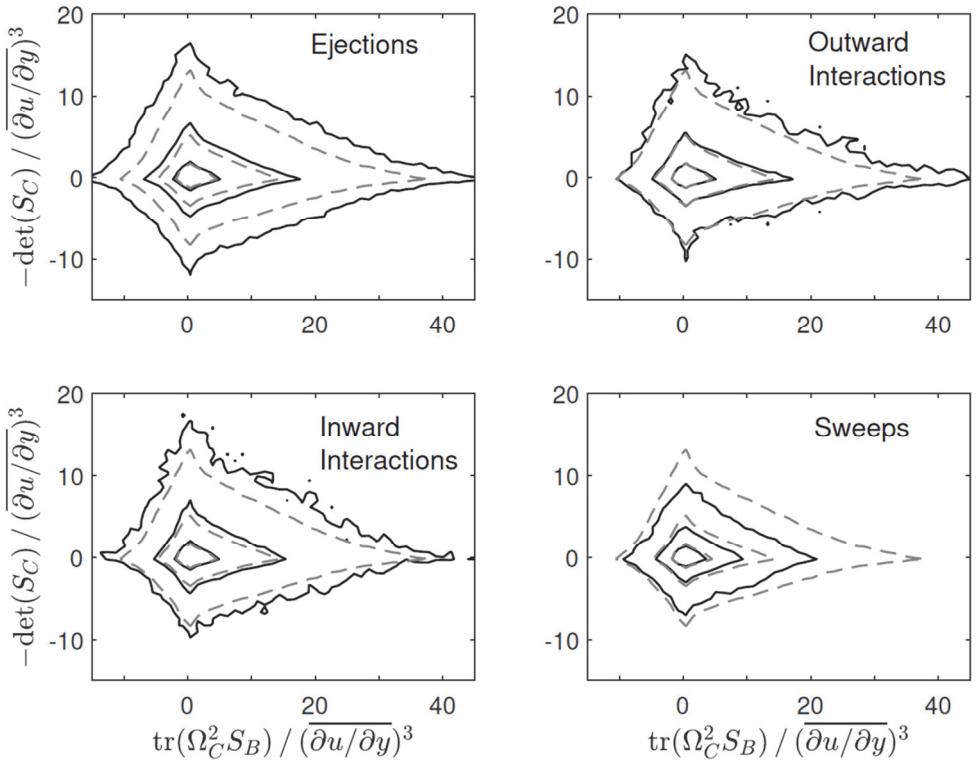

Fig. 8 The joint PDFs for the non-normal and interaction production terms for $60 \le y^+ \le 70$. Results are shown for the base 10 logarithms of the probabilities with contours from –4 to –2 in unit increments and each panel shows the results for the quadrants (solid, black lines) as well as all the data (grey, dashed lines)

eigenvalues for $\boldsymbol{A}$ form a conjugate pair and a real value, the eigenvalues for the normal straining consist of a pair of values equal to the real part of the conjugate pair, and a real value of opposite sign and double the magnitude[12]. In regions 1 and 5 the pair are positive values (the straining forms disc-like structures) while in regions 2 and 3 they are negative (forming tube-like structures). As a consequence, in Fig. 9 we only show results for regions 1, 2, 3 and 5 for the most positive and most negative eigenvalues (black line and light grey line, respectively) as the results for the intermediate eigenvalue (grey line) are identical to one of these. As a consequence of all the eigenvalues being real, and therefore distinct, the results for regions 4, 6 are a little more complex. Hence, additional panels at the bottom of Fig. 9 highlight $\cos(\theta_i^{CB}) > 0.9$ for these two regions.

The typical situation in all regions except region 2 is for there to be an alignment between $\boldsymbol{\omega}_C$, e_1, and anti-alignment between $\boldsymbol{\omega}_C$, e_3. It is also the case that the results for the ejections (solid lines) are rarely distinguishable from the dataset as a whole (dot-dashed lines). In contrast, in all regions except region 1 (where sweeps are rare) we see that the sweeps have a weaker alignment and anti-alignment; they have a more uniform PDF. Hence, an explanation for the enhanced contraction of the joint PDF for the sweeps along the abscissa in Fig. 8 relative to the ordinate is due to the fact that there is a weaker coupling between the normal straining and non-normal vorticity for sweeps. With the tendency to more positive values for κ_{BC} seen in Fig. 4 higher into the flow, particularly in regions 3-6 where the sweeps are more prevalent, we may state that sweeps not only have reduced non-normality and greater normal straining but a decoupling between these two terms. The consequence is that the surrounding vortical motions have a reduced impact on the mechanics of sweeping as a consequence of reduced non- normality (Figs. 4 and 5), with direct consequences for a reduction in combined non-normal production and interaction production (Fig. 8). The latter is particularly depleted because of the weaker coupling seen in Fig. 9.

We can compare the nature of the production terms in the log-layer with the flow nearer the wall at $20 < y^+ < 30$ through an examination of Figs. 10 and 11 compared to Figs. 7 and 8. The first of the two most noticeable features of Fig. 10 compared with Fig. 7 concerns the outward interactions: there is an extended positive sum for the normal production terms when the sum of the non-normal and interaction production terms is approximately zero. It was already noted that there is an extended tail to the top-right

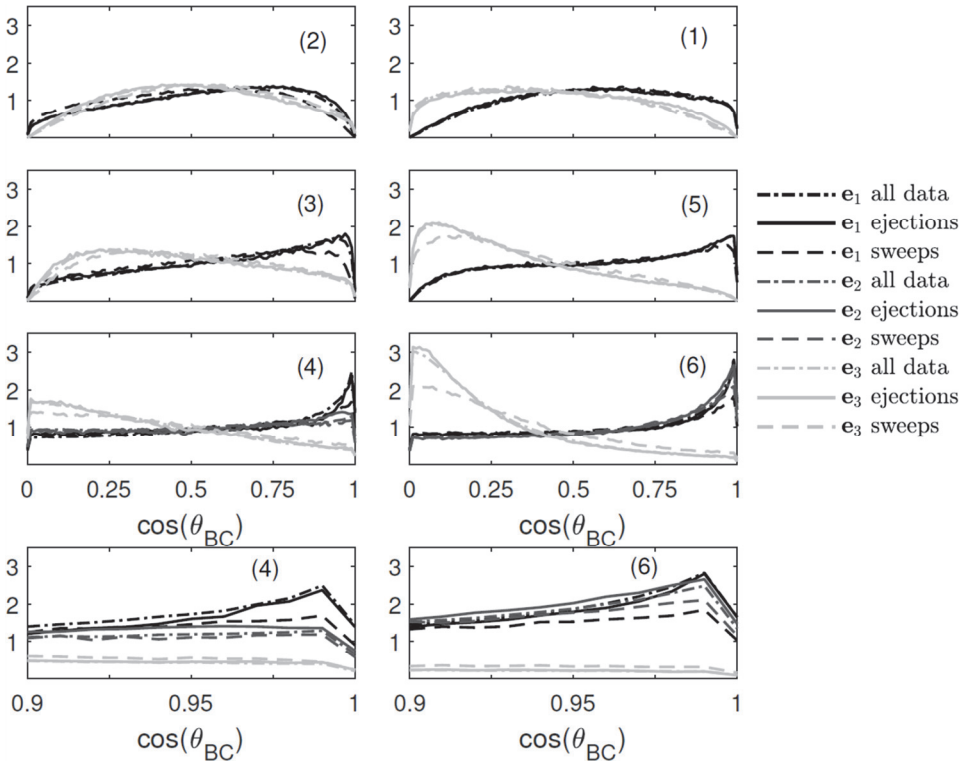

Fig. 9 Histograms for the cosine of the angle between the vorticity vector, $\boldsymbol{\omega}_C$, and the various eigenvectors of the normal straining (different shades of line) as a function of the region of the Q-R diagram (different panels) for $60 < y^+ < 70$. The results for all data are shown with a dot-dashed line, ejections with a solid line and sweeps as a dashed line. The bottom two panels highlight the $\cos(\theta_i^{CB}) > 0.9$ region. Note that for the regions where $\Delta > 0$ the intermediate and most positive normal strain eigenvalues are identical where $R > 0$ and the intermediate and most negative normal strain eigenvalues are identical where $R < 0$

quadrant of Fig. 6 in the panel for the outward interactions. Given that positive Q means that $\|\boldsymbol{\Omega}_B\|^2$ is large relative to $\|\boldsymbol{S}_B\|^2$ and that positive Φ means that the normal terms are greater in magnitude than the non-normality, then the implication is that locally generated enstrophy is dominating the outward interactions at this height. Figure 10 clarifies this result by indicating that the normal production effects associated with these outward interactions arise with minimal production from the non-normality–the outward interaction dynamics are local at these y^+.

The other dominant feature in Fig. 10 concerns the sweeps: there is a contraction in the x-axis for values of the y-axis close to zero. Thus, while normal production is enhanced for outward interactions where the non-normal and interaction production sum to zero, non-normal and interaction production are reduced when normal production is zero for sweeps. This parallels the result seen in Fig. 6 where the sweeps exhibit a contraction along the negative Φ axis for $Q \sim 0$. That the effects seen in Figs. 6 and 10 are not evident in Figs. 5 and 7 show that they are a consequence of the flow dynamics of the transitional region. The sweeps in Fig. 11 contrast with those in Fig. 8 by showing a more similar degree of contraction for both the non-normal production and the interaction production. The implication then that the decoupling between $\boldsymbol{\omega}_C$, e_1 is a feature of the logarithmic region that is less developed in the transitional region.

4. Conclusions

Understanding the dynamics of the velocity gradient tensor (VGT) is central to enhancing our knowledge of the processes by which turbulent flows transport momentum and dissipate energy. In the last four years, the Schur transform of the VGT has emerged worldwide as an alternative to the conventional Cauchy-Stokes or Hermitian/ skew-Hermitian decomposition of the VGT into rotational and straining components. There have been three primary strands to such work: The development of the concept of a real Schur flow, with applications of particular relevance to rotational and compressible flows[15, 42], the development of a coherent flow structure identifi-

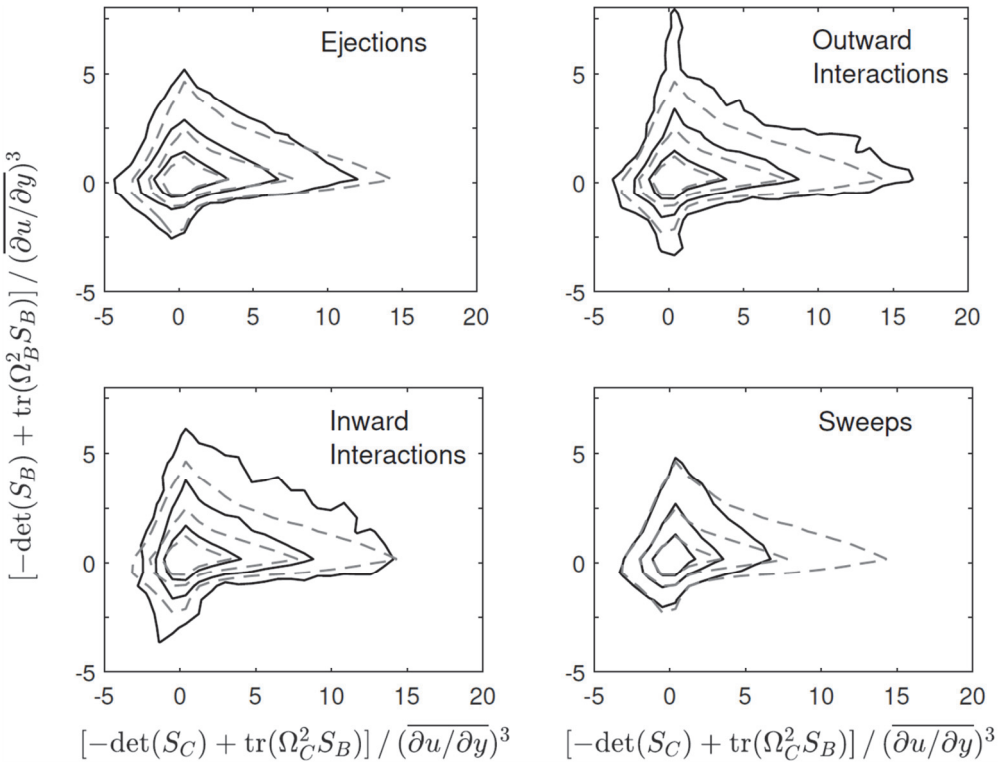

Fig. 10 The joint PDFs for sum of the normal and non-normal production terms for $20 \le y^+ \le 30$. Results are shown for the base 10 logarithms of the probabilities with contours from –4 to –2 in unit increments and each panel shows the results for the quadrants (solid, black lines) as well as all the data (grey, dashed lines)

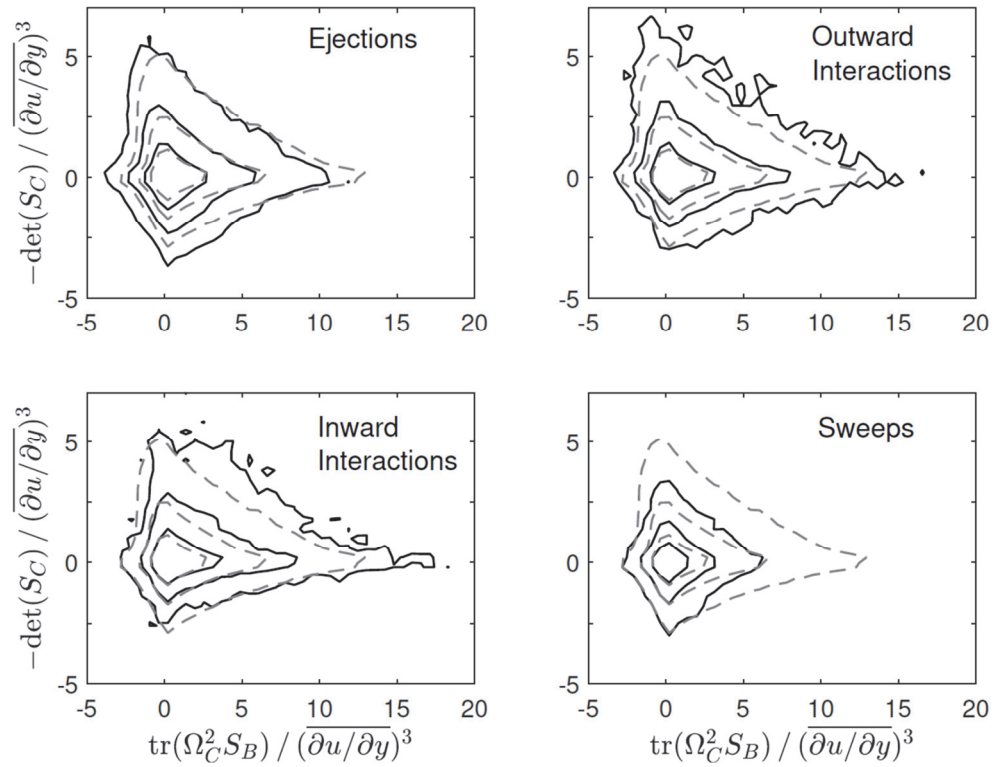

Fig. 11 The joint PDFs for the non-normal and interaction production terms for $20 \le y^+ \le 30$. Results are shown for the base 10 logarithms of the probabilities with contours from –4 to –2 in unit increments and each panel shows the results for the quadrants (solid, black lines) as well as all the data (grey, dashed lines)

cation method[13], with more recent work extending this to a decomposition of the kinematics of the VGT[46], and the combined use of the Schur decomposition and the Hermitian/ skew-Hermitian decomposition to expand the standard equations into components that represent the local and non-local dynamics within the flow[12]. This is an important property of the Schur decomposition as it gives the decomposition a clear physical meaning. This may be demonstrated by examining the nature of Cantwell's restricted Euler equations[30] shown in Eq. (15), where the dynamics may be written in terms of the eigenvalues of the VGT and incorporate the isotropic part of the pressure Hessian, and then noting that apart from the viscosity, the only term missing from the Cantwell model that features in Eq. (13) is the deviatoric part of the pressure Hessian, which may be shown to act non-locally[32].

In this paper we have focussed on the latter approach. In particular, we have applied this formalism to a direct numerical simulation of the near-wall region of a turbulent channel flow[52]. The non-Gaussian nature of the probability distributions for the VGT is classically seen in the "tear-drop shape"of the joint PDF for the second and third invariants, Q and R. We reveal an alternative source of non-Gaussianity by plotting Q against a term Φ that represents the difference between the sum of the normal, local terms (contained in Q) and the non-normal, non-local terms (Fig. 5). We then examined the relation between the VGT and the ejection and sweep events that make up the dominant motions in a boundary-layer. We found that it was the sweeps that have a particularly distinctive character compared to the flow field in general. In our Q-Φ diagram this can be seen in a truncation in the probability of negative Φ values for Q close to zero. Sweeps are particularly likely to arise where normal straining exceeds normal enstrophy[29]. In such regions and in the viscous sub-layer near the wall, the sweeps are likely to be dominated by the non-normal terms. However, in the transitional and logarithmic regions of the velocity profile, the sweeps are more likely to be dominated by normal dynamics than the flow in general or the other three flow quadrants (Fig. 4).

The reduction in the non-normality for the sweeps is reflected in the production terms, where there is a reduced contribution to the production budget from the terms involving the non-normality for the sweeps (Fig. 7). However, there is a difference between the logarithmic and transitional regions for the sweeps, with a particular reduction in the production term involving contributions from both the normal and non-normal terms relative to the purely non-normal production term in the logarithmic region (Fig. 8). The reason for this is a reduction in the degree of alignment between the non-normal vorticity vector and the eigenvector corresponding to the most positive eigenvalue of the normal strain rate tensor for the sweeps in the regions where they are most common.

The results presented here show how the Schur decomposition can uncover the dynamical richness of turbulent channel flow boundary-layers, as it places emphasis on the interplay between the local dynamics governed by the eigenvalues as well as the non-local dynamics related to the deviatoric part of the pressure Hessian. Furthermore, with attempts emerging to make use of this approach in practical subgrid-scale model closures for large-eddy simulation[33], it would appear that this is a rich area for future research.

References

[1] Escauriaza C., Paola C., Voller V. R. Computational models of flow, sediment transport and morphodynamics in rivers (Gravel-bed rivers: Process and disasters) [M]. New York, USA: John Wiley and Sons, 2017, 1-31.

[2] Keylock C. J., Hardy R. J., Parsons D. R. et al. The theoretical foundations and potential for large-eddy simulation (LES) in fluvial geomorphic and sedimentological research [J]. *Earth-Science Reviews*, 2005, 71(3-4): 271-304.

[3] Rodi W., Constantinescu G., Stoesser T. Large eddy simulation in hydraulics [C]. *Proceedings of 2013 IAHR (The International Association for Hydro-Environment Engineering and Research) World Congress*, Beijing, China, 2013.

[4] Stoesser T. Large-eddy simulation in hydraulics: Quo Vadis? [J]. *Journal of Hydraulics Research*, 2014, 52(4): 441-452.

[5] Constantinescu G. LE of shallow mixing interfaces: A review [J]. *Environmental Fluid Mechanics*, 2014, 14(5): 971-996.

[6] Smagorinsky J. General circulation experiments with the primitive equations. I. The basic experiment [J]. *Monthly Weather Review*, 1963, 91(3): 99-164.

[7] Nezu I. Open-channel flow turbulence and its research prospect in the 21st century [J]. *Journal of Hydraulic Engineering, ASCE*, 2005, 131(4): 229-246.

[8] Adrian R. J., Marusic I. Coherent structures in flow over hydraulic engineering surfaces [J]. *Journal of Hydraulics Research*, 2012, 50(5): 451-464.

[9] Keylock C. J. Flow resistance in natural, turbulent channel flows: The need for a fluvial fluid mechanics [J]. *Water Resources Research*, 2015, 51(6): 4374-4390.

[10] Meneveau C. Lagrangian dynamics and models of the velocity gradient tensor in turbulent flows [J]. *Annual Reviews of Fluid Mechanics*, 2011, 43: 219-245.

[11] Li Z., Zhang X. W., He F. Evaluation of vortex criteria by virtue of the quadruple decomposition of velocity gradient tensor [J]. *Acta Physica Sinica*, 2014, 63(5): 054704.

[12] Keylock C. J. The Schur decomposition of the velocity gradient tensor for turbulent flows [J]. *Journal of Fluid Mechanics*, 2018, 848: 876-904.

[13] Liu C., Gao Y., Tian S. et al. Rortex–A new vortex vector definition and vorticity tensor and vector decompositions [J]. *Physics of Fluids*, 2018, 30(3): 035103.
[14] Gao Y., Liu C. Rortex and comparison with eigenvalue-based vortex identification criteria [J]. *Physics of Fluids*, 2018, 30(8): 85107.
[15] Zhu J. Z. Vorticity and helicity decompositions and dynamics with real Schur form of the velocity gradient [J]. *Physics of Fluids*, 2018, 30: 031703.
[16] Suman S., Girimaji S. S. Velocity gradient invariants and local flow-field topology in compressible turbulence [J]. *Journal of Turbulence,* 2010, 11: N2.
[17] Danish M., Suman S., Srinivasan B. A direct numerical simulation-based investigation and modeling of pressure Hessian effects on compressible velocity gradient dynamics [J]. *Physics of Fluids*, 2014, 26(12): 126103.
[18] Hunt J., Wray A., Moin P. Eddies, streams, and convergence zones in turbulent flows [R]. Proceedings of the Summer Program. Center for Turbulence Research, 1988, 193-208.
[19] Khosronejad A., Sotiropoulos F. Numerical simulation of sand waves in a turbulent open channel flow [J]. *Journal of Fluid Mechanics*, 2014, 753: 150-216.
[20] McSherry R. J., Chua K. V., Stoesser T. Large eddy simulation of free-surface flows [J]. *Journal of Hydrodynamics*, 2017, 29(1): 1-12.
[21] Marjoribanks T. I., Hardy R. J., Lane S. N. et al. Does the canopy mixing layer model apply to highly flexible aquatic vegetation? Insights from numerical modelling [J]. *Environmental Fluid Mechanics*, 2017, 17: 277-301.
[22] Chong M. S., Perry A. E., Cantwell B. J. A general classification of three-dimensional flow fields [J]. *Physics of Fluids A, Fluid Dynamics*, 1990, 2(5): 765-777.
[23] Lund T. S., Rogers M. M. An improved measure of strain state probability in turbulent flows [J]. *Physics of Fluids*, 1994, 6(5): 1838-1847.
[24] Li Y., Meneveau C. Material deformation in a restricted Euler model for turbulent flows: Analytic solution and numerical tests [J]. *Physics of Fluids*, 2007, 19(1): 015104.
[25] Tsinober A. Vortex stretching versus production of strain/ dissipation (Turbulence structure and vortex dynamics) [M]. Cambridge, UK: Cambridge University Press, 2001, 164-191.
[26] Vieillefosse P. Internal motion of a small element of fluid in an inviscid flow [J]. *Physica A*, 1984, 125(1): 150-162.
[27] Laizet S., Nedíc J., Vassilicos C. Influence of the spatial resolution on fine-scale features in DNS of turbulence generated by a single square grid [J]. *International Journal of Computational Fluid Dynamics*, 2015, 29(3-5): 286-302.
[28] Beaumard P., Buxton O. R. H., Keylock C. J. The importance of non-normal contributions to velocity gradient tensor dynamics for spatially developing, inhomogeneous, turbulent flows [J]. *Journal of Turbulence*, 2019, 20(9): 577-598.
[29] Chacin J. M., Cantwell B. J. Dynamics of a low Reynolds number turbulent boundary layer [J]. *Journal of Fluid Mechanics*, 2000, 404: 87-115.
[30] Cantwell B. J. Exact solution of a restricted Euler equation for the velocity gradient tensor [J]. *Physics of Fluids A*, 1992, 4: 782-793.
[31] Zhu J. Z. Real Schur flow computations, helicity fastening effects and Bagua-pattern cyclones [J]. *Physics of Fluids*, 2021, 33: 107112.
[32] Ohkitani K., Kishiba S. Nonlocal nature of vortex stretching in an inviscid fluid [J]. *Physics of Fluids*, 1995, 7(2): 411-421.
[33] Yu J. L., Zhao Z., Lu X. Y. Non-normal effect of the velocity gradient tensor and the relevant subgrid-scale model in compressible turbulent boundary layer [J]. *Physics of Fluids*, 2021, 33: 025103.
[34] Germano M., Piomelli U., Moin P. et al. A dynamic subgrid-scale eddy viscosity model [J]. *Physics of Fluids A*, 1991, 3(7): 1760-1765.
[35] Kerr R. M. Higher-order derivative correlations and the alignment of small-scale structures in isotropic numerical turbulence [J]. *Journal of Fluid Mechanics,* 1985, 153: 31-58.
[36] Ashurst W. T., Kerstein A. R., Kerr R. A. et al. Alignment of vorticity and scalar gradient with strain rate in simulated Navier-Stokes turbulence [J]. *Physics of Fluids*, 1987, 30(8): 2343-2353.
[37] Taylor G. I. The spectrum of turbulence [J]. *Proceedings of the Royal Society of London, Series A*, 1938, 164: 476-490.
[38] Betchov R. An inequality concerning the production of vorticity in isotropic turbulence [J]. *Journal of Fluid Mechanics*, 1956, 1: 497-504.
[39] Boukharfane R., Er-raiy A., Parsani M. et al. Structure and dynamics of small-scale turbulence in vaporizing two-phase flows [J]. *Scientific Reports*, 2021, 11: 15242.
[40] Lee S. L. A practical upper bound for departure from normality [J]. *SIAM Journal of Matrix Analysis and Applications*, 1995, 16(2): 462-468.
[41] Keylock C. J. Turbulence at the Lee bound: Maximally non-normal vortex filaments and the decay of a local dissipation rate [J]. *Journal of Fluid Mechanics*, 2019, 881: 283-312.
[42] Zhu J. Z. Thermodynamic and vortic structures of real Schur flows [J]. *Journal of Mathematical Physics*, 2021, 62: 083101.
[43] Zhu J. Z. Compressible helical turbulence: Fastened-structure geometry and statistics [J]. *Physics of Plasmas*, 2021, 28(3): 032302.
[44] Dong X., Gao Y., Liu C. New normalized Rortex/ vortex identification method [J]. *Physics of Fluids*, 2019, 31(1): 011701.
[45] Xu H., Cai X. S., Liu C. Liutex (vortex) core definition and automatic identification for turbulence vortex structures [J]. *Journal of Hydrodynamics*, 2019, 31(5): 857-863.
[46] Liu C., Yu Y., Gao Y. Liutex based new fluid kinematics [J]. *Journal of Hydrodynamics*, 2022, 30(3): 355-371.
[47] Lu S. S., Willmarth W. W. Measurements of the structure of the Reynolds stress in a turbulent boundary layer [J]. *Journal of Fluid Mechanics*, 1973, 60: 481-511.
[48] Nakagawa H., Nezu I. Prediction of the contributions to the Reynolds stress from bursting events in open channel flows [J]. *Journal of Fluid Mechanics*, 1977, 80: 99-128.
[49] Keylock C. J., Lane S. N., Richards K. S. Quadrant/octant sequencing and the role of coherent structures in bed load sediment entrainment [J]. *Journal of Geophysical Research*, 2014, 119: 264-286.
[50] Wan M., Chen S., Eyink G. et al. Johns Hopkins Turbulence Database (JHTDB) [EB/OL]. 2016, http://turbulence.pha.jhu.edu/datasets.aspx.
[51] Li Y., Perlman E., Wan M. et al. A public turbulence database cluster and applications to study Lagrangian evolution of velocity increments in turbulence [J]. *Journal of Turbulence*, 2008, 9: N31.
[52] Graham J., Kanov K., Yang X. et al. A web services

accessible database of turbulent channel flow and its use for testing a new integral wall model for LES [J]. *Journal of Turbulence*, 2016, 17(2): 181-215.

[53] Lee M., Malaya N., Moser R. Petascale direct numerical simulation of turbulent channel flow on up to 786k cores [C]. *2013 SC-International Conference for High Performance Computing, Networking, Storage and Analysis*, Denver, CO, USA, 2013.

[54] Comte-Bellot G., Sabot J., Saleh I. Detection of intermittent events maintaining Reynolds stress [C]. *Proceedings of the Dynamics of Flow Conference–Dynamic Measurements in Unsteady Flows*, Marseille, France, 1978, 213.

[55] Bogard D. G., Tiederman W. G. Burst detection with single-point velocity measurements [J]. *Journal of Fluid Mechanics*, 1986, 162: 389-413.